Fatigue crack propagation: In situ visualization using X-ray microtomography and 3D simulation using the extended finite element method

Emilie Ferrié, Jean-Yves Buffière, Wolfgang Ludwig, Anthony Gravouil, Lyndon Edwards

Fatigue crack propagation: In situ visualization using X-ray microtomography and 3D simulation using the extended finite element method

Emilie Ferrié [a], Jean-Yves Buffière [a,*], Wolfgang Ludwig [a], Anthony Gravouil [b], Lyndon Edwards [c]

[a] *Groupe d'Etude de Métallurgie Physique et de Physique des Matériaux, INSA de Lyon, 25 av. Jean Capelle, 69621 Villeurbanne Cedex, France*
[b] *Laboratoire de Mécanique des Contact et des Solides, INSA de Lyon, 69621 Villeurbanne, France*
[c] *Department of Materials Engineering, The Open University, Milton Keynes, UK*

The propagation of a semi-elliptical crack in the bulk of an ultrafine-grained Al–Li alloy has been investigated using synchrotron radiation X-ray microtomography. In this material, the studied crack, despite its small dimension, can be considered as "microstructurally long" and described in the frame of the linear elastic fracture mechanics. The extended finite element method is used to calculate the stress intensity factors along the crack front taking into account the three-dimensional geometry extracted from the tomographic images. For the same nominal value of the stress intensity factor range, crack propagation is faster in the bulk than at the surface. The observed anisotropy is attributed to the variation of the closure stress along the crack front between surface and bulk. The experimentally observed fatigue crack propagation is compared to numerical simulations. Good agreement is found when a linear variation of closure stress along the crack front is taken into account in the "3D crack propagation law" used for the simulation.

Keywords: Fatigue crack propagation; Extended finite element method; Synchrotron radiation; Microtomography; Crack closure

1. Introduction

In the last 20 years, efforts have been made to develop experimental techniques for investigating the behaviour of fatigue cracks *within the bulk* of opaque materials. For instance, indirect techniques such as direct (or alternating) current potential drop measurement [1–3], Rayleigh wave resonance [4] or compliance measurements [5] have all been used to estimate the size of fatigue cracks in bulk samples. However, no information is obtained on the three-dimensional (3D) shape of the crack inside these samples and the estimates given by these techniques are sensitive to several factors such as the crack/probe distance [2] or the presence of residual stress [3]. More quantitative information on crack front shape evolution can be obtained by means of post-mortem fractographic techniques such as heat tinting [6], the "marker technique" [7] or the more widely used "beach marking technique" [8]. This latter technique consists of increasing, during a certain number of fatigue cycles, the minimum cycling stress while the value of the maximum stress is kept constant. By doing so, a distinguishable striation-free area is created on the fracture surface which allows the crack shape to be later determined. However, this technique assumes that changing the stress amplitude during the load cycle, without changing the maximum load value, does not alter the crack shape. The validity of this assumption remains questionable. Furthermore, in Al alloys, fracture surface markings obtained close to the sample surface are blurred so that the crack shape

* Corresponding author. Tel.: +33 4 72 73 88 54; fax: +33 4 72 43 85 39.
E-mail address: Jean-Yves.Buffiere@insa-lyon.fr (J.-Y. Buffière).

can only be determined using optical profile measurement techniques [9]. These experimental methods have mainly been used to study the shape evolution of *part-through cracks*, which are, for most cases, more representative of cracks in real structures than through cracks. Fractographic observations of samples subjected to mode I (or mode II) loading have shown that the shape of part-through cracks is usually near to semi-elliptical [9,10].

Alongside these characterisation methods, analytical models predicting 3D fatigue crack growth of part-through cracks in specimens with simple geometries (usually plates) have also been developed, for example in Ref. [11]. They are normally based on the overarching assumption that the crack has a semi-elliptical shape so that crack extension may be calculated at the surface and at the depth using analytical stress intensity factor equations established for tensile or bending loading [12] or polynomial stress distributions [13]. Three-dimensional finite element (FE) calculations have also been used intensively to simulate crack propagation in more complex crack/specimen/loading configurations. Load spectrum effects have been investigated [14] and propagation of non-planar cracks under mixed-mode conditions has been predicted [15,16].

However, direct comparisons between the crack front shape observed experimentally and that simulated by the FE method are rather limited: final crack shape [15,16] or beach marks [17] observed on the fracture surface have been compared to 3D FE results and discrepancies were found at the surface. Crack sizes obtained by 3D FE simulations for different configurations have also been compared to experimental results [18] and an error of 30% was found in the predicted crack shape evolution. Whichever method is used for crack propagation simulation, analytical or numerical, the local crack extension at the surface and also in the bulk is calculated using Paris law equations based on fatigue crack growth measurements at the specimen surface. This means that simulations of the crack front shape evolution, and, indirectly, the prediction of the fatigue lifetime of the component or structure, are based on the assumption that the crack growth behaviour measured at the surface can account for crack growth behaviour in the bulk. This assumption is necessary due to the lack of reliable quantitative experimental data describing *long crack propagation* in the *bulk* of structural materials.

The aim of the study presented here is to observe experimentally long crack propagation in the bulk of metallic alloys and to predict the crack shape evolution using linear elastic fracture mechanics (LEFM). Synchrotron radiation X-ray microtomography is used to investigate in three dimensions the development of a semi-elliptical crack in an ultrafine-grained Al alloy. This high-resolution 3D imaging technique allows the 3D structure of objects in the bulk of a non-transparent material to be visualised with a resolution close to 1 μm. At such a resolution, the maximum volume that can be imaged is 1 mm^3. Due to this size limitation, the observation of crack propagation in conventional metallic alloys, with a grain size in the range of 10–100 μm, is limited to the short crack regime. Microstructurally short cracks have already been investigated in coarse-grained cast Al alloys [19] and in cast iron [20]. Short cracks are strongly influenced by microstructural features such as grain boundaries and exhibit multiple branching so that no modelling of the 3D propagation has been attempted yet.

In the fine-grained alloy studied here, the crack size (which is in the range 100–500 μm) is at least 100 times the grain size, and can hence be considered as *microstructurally long* as defined by Miller [21]. The extended FE method (X-FEM) is used to calculate the stress intensity factors along the crack front taking into account the real 3D geometry of the crack extracted from the tomographic images. Based on experimental observations and quantitative analysis of crack propagation in the bulk, a "3D crack growth law" is established to predict the crack front shape evolution in the bulk of the material.

2. Experimental

2.1. Material

The material used in this study is a powder metallurgy Al–Li alloy based on AA5091 alloy obtained from Aerospace Metal Composites Ltd, UK. The alloy composition was Al–4.0Mg–1.2Li–1.0C–0.5O and was produced from powders using a mechanical alloying process, followed by hot isostatic pressing (hipping) [22]. The billet was supplied as an upset forged 42 mm thick plate in the as-forged (T1) condition. The material exhibited a yield stress of 450 MPa and a tensile strength of 505 MPa, values similar to those previously reported for 5091 in the T1 condition [22–24]. The tensile performance of Al–Mg–Li–C alloys is derived from significant Hall–Petch strengthening, due to their very fine-grain structure, solution and dispersion hardening. They typically possess a high Mg concentration in comparison to heat treatable Al–Li alloys, but the Li concentration is deliberately kept below 1.5%, to prevent formation of the age hardening δ' phase (Al_3Li). During the mechanical alloying, surface layers of oxides on the powder particles are repeatedly grown, then fractured and dispersed within the particles. The grains, which are typically smaller than 1 μm, contain significant distributions of fine (50–100 nm) precipitates, which are believed to be Al_4C_3, Al_2O_3 and MgO. The Al_2O_3 and MgO phases derive from fragmentation of the surface oxides from the as-received materials. The Al_4C_3 phase, by contrast, derives only from the reaction between the aluminium and the process control agent used to aid the sintering process [25].

The main advantage of using this alloy for the present study is that it exhibits an exceptionally linear crack path compared to ingot metallurgy Al alloys. The ultrafine grains promote homogeneous deformation and prevent crystallographic cracking so that the crack shape is not disturbed by microstuctural features, at least not at the level of the spatial resolution employed in this study. This fine

microstructure also endows the alloy with low levels of crack closure [23,25] and yield stress-insensitive fatigue crack propagation behaviour so that the properties of the as-forged T1 materials [23,27] are indistinguishable from those of the fully heat treated condition [26].

2.2. X-ray microtomography: a 3D imaging technique

In situ fatigue tests monitored by X-ray microtomography were carried out on beamline ID 19[1] of the European synchrotron radiation facility (ESRF) in Grenoble, France. This experimental station is dedicated to high-resolution X-ray imaging and features a highly coherent X-ray beam, a precision mechanics sample stage and a high-resolution detector system. The latter consists of a 2024^2 CCD camera coupled via microscope optics to a scintillator that transforms X-ray photons into visible light. In the work presented here, a multilayer crystal is used to monochromatise the incoming white beam to an energy of 20.5 keV. This value allows imaging of Al samples of millimetric dimensions. During a tomographic scan, the sample is rotated over 180° in order to acquire 1500 two-dimensional (2D) projection radiographs. From this set of projections, a quantitative 3D map of the attenuation coefficient distribution within the sample is produced by means of a standard filtered backprojection tomographic reconstruction algorithm. The spatial resolution obtained in the reconstructed images is of the order of 1 μm, a value comparable to the resolution of an optical microscope. Due to the coherence of the X-ray beam, the tomographic images contain, in addition to conventional "absorption contrast", a "phase contrast" contribution due to propagation and Fresnel diffraction of the highly coherent wavefield over the finite specimen/detector distance. This phase contrast results in an edge enhancement and is particularly useful for visualising small details for which the "absorption contrast" is very low [28]. In our case, it improves crack-tip detection [19]. However, a too strong phase contrast will tend to spoil the resolution and lead to reconstruction artefacts. For this reason, the phase contrast contribution, is controlled by adjusting the specimen/detector distance so that the diffraction fringes only appear locally at the edges of heterogeneities.

2.3. Fatigue machine and specimen geometry

The sample was imaged in a dedicated fatigue machine designed at INSA Lyon to perform in situ fatigue test at the ESRF. Its specific features are the following: the load frame consists of a poly(methyl methacrylate) tube nearly transparent to X-rays such that the sample, under load, is visible over 180° during the scan acquisition. The mechanical design of the cyclic tension loading mechanism enables operation at cycling frequencies of up to 80 Hz, minimising thereby the cycling time required for a fatigue test. This is a crucial point as, for a given experiment, the average beamline availability is 72 h. The compact design of the device and the low vibration level enabled us to directly mount it on the sample stage of the tomograph of beamline ID19. (A more detailed description can be found in Ref. [29].)

At the spatial resolution employed (0.7 μm pixel size), and in parallel beam configuration, the maximum gauge volume is limited by the detector area and amounts to approximately 1.4 mm^3. Small fatigue specimens with a minimum cross-section of 1 mm × 1 mm were spark cut from a piece of as-forged 5091 material. The geometry of the sample used is represented in Fig. 1(a). A thin (2 μm) rectangular notch, 100 μm wide and 20 μm deep, was produced in the sample using focused ion beam machining and is represented in Fig. 1(b). This notch is located at the centre of one of the specimen faces and acts as a crack initiation site.

2.4. Fatigue experiment

An in situ fatigue test was performed in air, at constant stress amplitude with $\sigma_{max} = 220$ MPa, a stress ratio $R = 0.1$, a frequency of 40 Hz and at room temperature. The value of σ_{max} was chosen such that the stress intensity factor calculated at the surface of a semi-circular crack with a 100 μm radius is 2.86 MPa $m^{1/2}$ which is close to the long crack threshold value of 2.7 MPa $m^{1/2}$ given in Ref. [26]. Crack initiation was monitored by simple 2D radiographs acquired at regular intervals. Once a crack was detected, tomographic scans were recorded regularly (every 1000 or 2000 cycles) to monitor crack propagation in the bulk of the material. The specimen was imaged under

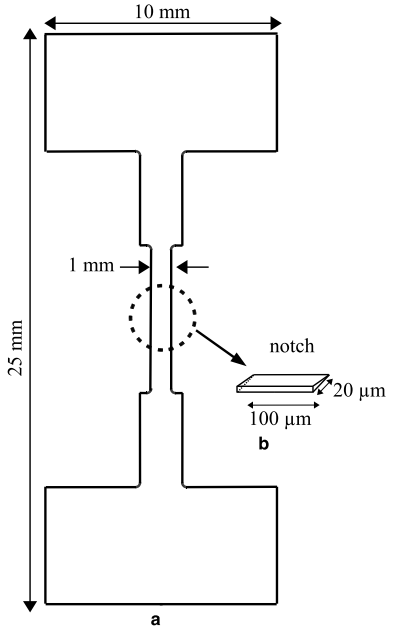

Fig. 1. (a) Geometry of the sample used for the in situ fatigue test monitored by X-ray microtomography. (b) 3D illustration of the notch obtained by focused ion beam machining and located at the centre of one of the specimen faces.

[1] Beamline ID19 website: http://www.esrf.fr/exp_facilities/ID19/homepage/id19homepage.html.

load such that the crack was fully open on the 3D images. After 18,000 fatigue cycles, a 100% tensile overload was applied. After this overload, the load level was set to its initial value ($\sigma_{max} = 220$ MPa with $R = 0.1$) and the fatigue experiment was continued until failure.

2.5. Processing of the tomographic images

Each tomographic 3D image acquired during the fatigue test shows the crack shape "inside" the aluminium alloy. Amira 3D imaging software was used to visualise the 3D raw images and also to perform the segmentation operation required to extract the crack from the surrounding microstructure [30]. Reconstruction artefacts due to phase contrast produce spurious images so that a manual segmentation operation had to be performed. Once extracted, the crack was defined as an independent object and its full 3D geometry was visualised on 3D renditions. As an illustration, the 3D rendition of the crack at 16,000 cycles is displayed in Fig. 2. In this figure, the two orthogonal images that intersect the crack are slices extracted from the reconstructed 3D tomographic images. The rectangular focused ion beam notch is indicated in the (X–Y) plane of the crack by black dotted lines.

2.6. Calculation of the local stress intensity factor values along the crack front

In this section, we present briefly the method used to calculate mixed-mode stress intensity factors (K_I, K_{II} and K_{III}) along the crack front obtained from the 3D tomographic images. The numerical technique presented here couples the X-FEM [31] with the level sets method [32], which is used to define the crack geometry.

2.6.1. Crack modelling by enrichment functions

In FE methods, the presence of cracks in a structure must be taken into account in mesh generation: the mesh must adequately define the crack geometry. Special elements and considerable mesh refinement near the crack tip are necessary to capture accurately the asymptotic displacement fields. The X-FEM alleviates the shortcomings associated with meshing the crack surface by representing the crack geometry using additional functions called enrichment functions. The enrichment method, as described in Ref. [33], can be summarised as follows. The displacement field calculated in the structure "without crack" is locally modified by adding, at specific nodes, the nodal values of the enrichment functions. These functions define the crack geometry by "modelling" the discontinuity introduced by the crack in the displacement field. As the discontinuities at the crack front and along the crack surface are different, two enrichment functions, named H and F_J, are necessary to model the entire crack.

The function H, defined as a generalised Heaviside function, models the displacement field along the crack surface. It is used to enrich the nodes of the element that are cut by the crack surface and can be defined as follows:

$$H(x) = \begin{cases} +1 & \text{for } \overrightarrow{(x - x^*)} \cdot \vec{n} \geqslant 0, \\ -1 & \text{otherwise.} \end{cases} \quad (1)$$

In Eq. (1), x is a given point of the (X, Y, Z) space, x^* is a point of the crack surface and $\vec{n}$ is a vector in x^* normal to the crack surface (see Fig. 3(a)).

The enrichment F_J is used to enrich the nodes of the elements that contain the crack front. F_J consists of a span of functions which incorporate the radial and angular behaviour of the asymptotic crack-tip displacement fields. F_J is given by the following equation where r and θ are expressed in the local polar coordinate system of the crack front [34] (see Fig. 3(a)):

$$\{F_J(\mathbf{x})\} \equiv \left\{ \sqrt{r}\sin\left(\frac{\theta}{2}\right), \sqrt{r}\cos\left(\frac{\theta}{2}\right), \sqrt{r}\sin\left(\frac{\theta}{2}\right)\sin(\theta), \sqrt{r}\cos\left(\frac{\theta}{2}\right)\sin(\theta) \right\}. \quad (2)$$

Fig. 3(b) illustrates the enrichment strategy in two dimensions when the crack is not aligned with the element edges. The key issue is now to define the 3D crack geometry independently of the mesh of the structure in order to select the nodes that must be enriched by H and F_J.

2.6.2. Implicit representation of the crack using the level sets method

The crack front is defined as the intersection between a surface $\Gamma_{surface}$ that defines the crack surface and a surface Γ_{front} that defines the crack front. These two surfaces, defined for a semi-elliptical crack, are displayed in Fig. 4.

In the general case, these surfaces can have arbitrary 3D shape, and are defined by means of level sets functions. The concept of level sets functions was initially introduced by Osher et al. to track moving interfaces [32]. A level sets function $\gamma(x)$ (where x is a point of the (X, Y, Z) space), used to represent an arbitrary surface Γ, can be defined as a scalar

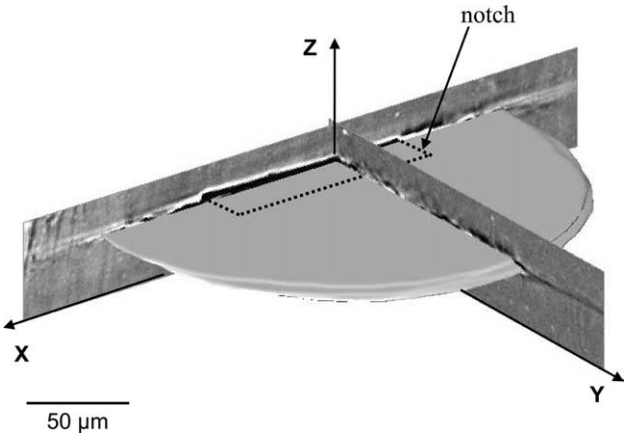

Fig. 2. 3D rendition of the crack after 16,000 cycles: the rectangle in black dotted lines represents the notch in the (X–Y) plane of the crack. The two orthogonal grey-scale images are slices along the (X–Z) and (Y–Z) planes extracted from the raw tomographic dataset.

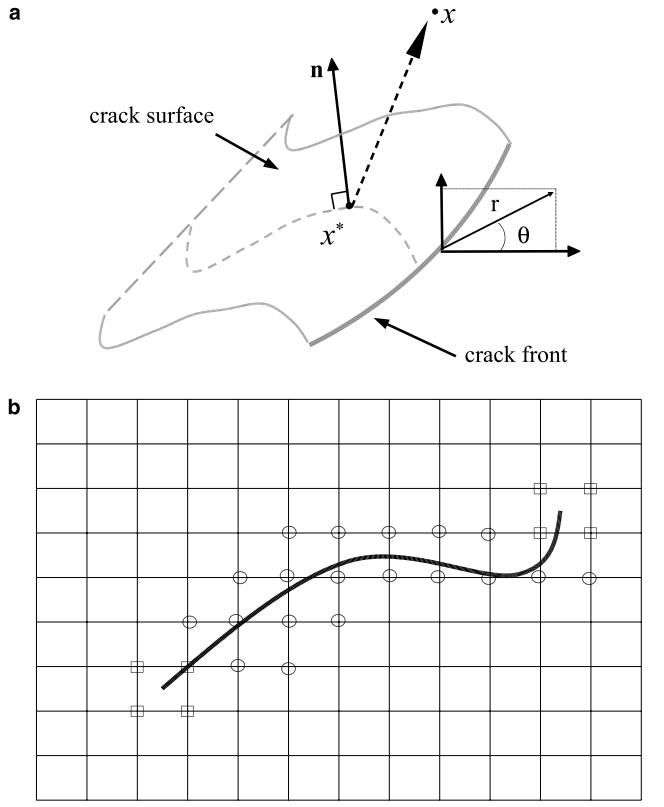

Fig. 3. (a) Part of the crack front and its local polar coordinate system used to express the enrichment function F_J and H as well as the displacement fields. The vector **n** is the normal in x^* to the crack surface, and x is a point of the (X, Y, Z) space inside the structure. (b) 2D schematic representation of the crack (black curve) and the mesh of the structure that contains the crack (squared grid). The nodes of elements cut by the crack are enriched by the H function and are represented by open circles. The nodes of the elements that contain the crack tip are enriched by the F_J functions span and are represented by open rectangles.

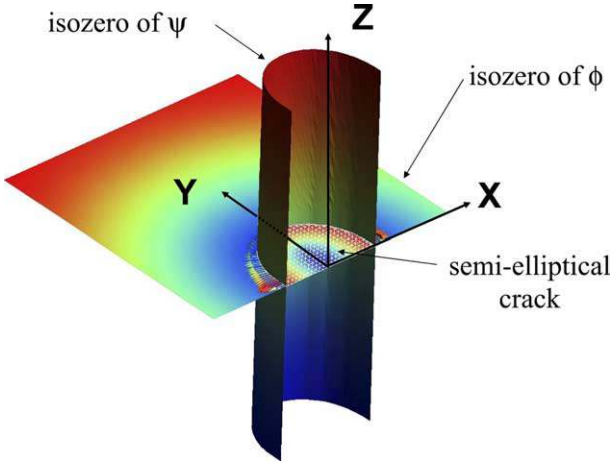

Fig. 4. The surface in the $(X–Y)$ plane is the iso-zero surface of the level set function $\phi(x)$ and represents the crack surface. The "curved" surface normal to the $(X–Y)$ plane is the iso-zero surface of $\psi(x)$ and represents the crack front, which corresponds to the intersection of these two iso-zero surfaces.

field, where each scalar is the signed distance to the surface Γ. Two level sets functions, ϕ and ψ, define the surfaces Γ_{surface} and Γ_{front}, respectively, which give the following equations:

$$\phi(x) = \pm\left\|x - x_{\Gamma_{\text{surface}}}\right\| \text{ where } x_{\Gamma_{\text{surface}}} \in \Gamma_{\text{surface}} \quad \text{and}$$
$$\psi(x) = \pm\left\|x - x_{\Gamma_{\text{front}}}\right\| \text{ where } x_{\Gamma_{\text{front}}} \in \Gamma_{\text{front}}, \tag{3}$$

Γ_{surface} is the iso-zero surface of the scalar field ϕ:$\phi(x) = 0$. Similarly, Γ_{front} is the iso-zero surface of ψ:$\psi(x) = 0$ see (Fig. 4).

The values of ψ and ϕ are stored at each node of the elements of the structure. The nodal values of ψ and ϕ give the precise location of the crack and control whether a node has to be enriched or not. In the study presented here, the level sets functions ψ and ϕ are built from the real crack shape obtained from the 3D tomographic image by calculating the signed distance function to Γ_{surface} and Γ_{front} using a C++ subroutine.

The values of the stress intensity factors, K_{I}, K_{II} and K_{III}, along 3D curved cracks are determined using a general crack-tip interaction integral introduced by Gosz and Moran [35]. Details concerning the calculation of the mixed-mode stress intensity factors can be found, for instance, in Refs. [33–35].

2.6.3. Advantage of the X-FEM

The numerical method used in this study is very general and allows the calculation of the stress intensity factors K_{I}, K_{II} and K_{III} for a crack with an arbitrary 3D geometry. Because of the addition of local enrichment functions, accurate values of the stress intensity factors can be obtained with a relatively coarse mesh compared to the mesh used at the crack tip in conventional FE methods. Moreover, the crack geometry and the FE mesh of the structure are defined separately, and no remeshing of the entire structure is necessary when the crack size/shape changes.

3. Results

After 14,000 fatigue cycles, a crack initiated at the notch was detected on a 2D radiograph. A tomographic scan of the part of the specimen containing the crack was acquired and corresponds to the "first scan". During crack propagation, nine scans were recorded, reconstructed and segmented to obtain 3D renditions of the crack at different stages of its evolution. Projections in the $(X–Y)$ plane of seven 3D renditions (chosen among the nine) are displayed in Fig. 5. The dotted lines on the 3D crack renditions represent the location of the crack front at the previous step. The position along the crack front is defined by the angle ω as shown in Fig. 5(a). Qualitative and quantitative information on the evolution of the 3D crack geometry obtained from the 3D renditions of the crack is presented in this section.

3.1. Crack shape evolution

The crack plane, as shown in Fig. 2, appears almost perfectly flat and is normal to the z axis which is parallel to the stress direction. The crack front shape remains close to a

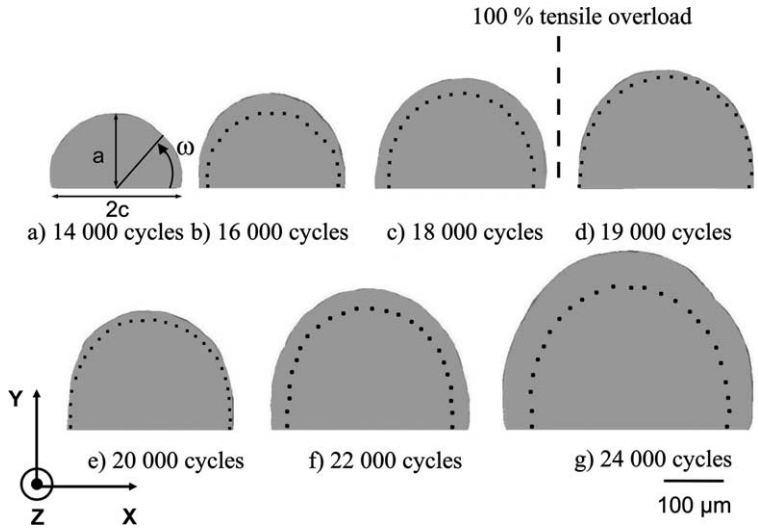

Fig. 5. Projections in the (X–Y) plane of 3D renditions of the crack at different stages of its development. (a) The angle ω is used to determine the location of a given point along the crack front. (b) The black dotted lines on the 3D rendition represent the location of the crack front at the previous stage (a), and similarly for stages (c)–(g).

semi-ellipse during crack propagation. The aspect ratio a/c, defined as the ratio of the crack depth a and the half surface length c, as defined in Fig. 5(a), is increasing steadily from 1.1 to 1.4 during crack growth (see Table 1). The effect of the 100% tensile overload on the crack front shape (see Fig. 5(d)) is discussed in Section 3.3.

Table 1
Evolution of the aspect ratio during crack propagation

N	14,000	16,000	18,000	19,000	20,000	22,000	24,000
a/c	1.19	1.23	1.29	1.35	1.37	1.39	1.44
				↑			
				100% tensile overload			

3.2. Fatigue crack growth rate at the surface and in the bulk

The crack size at the surface ($2c$), for $\omega = 0°$, and in the bulk (a), for $\omega = 90°$, are measured on the 3D renditions of the crack (see Fig. 5). The fatigue crack growth rates at the surface, $\mathrm{d}c/\mathrm{d}N$, and in the bulk, $\mathrm{d}a/\mathrm{d}N$, as a function of the stress intensity factor range $\Delta K = (K_{\max} - K_{\min})$ are shown in Fig. 6. The values of $K_{\max}$ and $K_{\min}$ are calculated for $\omega = 0°$ and for $\omega = 90°$ using the X-FEM presented in Section 2.6. Note that $K_{\max}$ and $K_{\min}$ are the stress intensity factor under mode I, the values of K_{II} and K_{III} are taken equal to 0 as the crack, subjected to uniaxial tension loading, is normal to the stress axis. For comparison, the

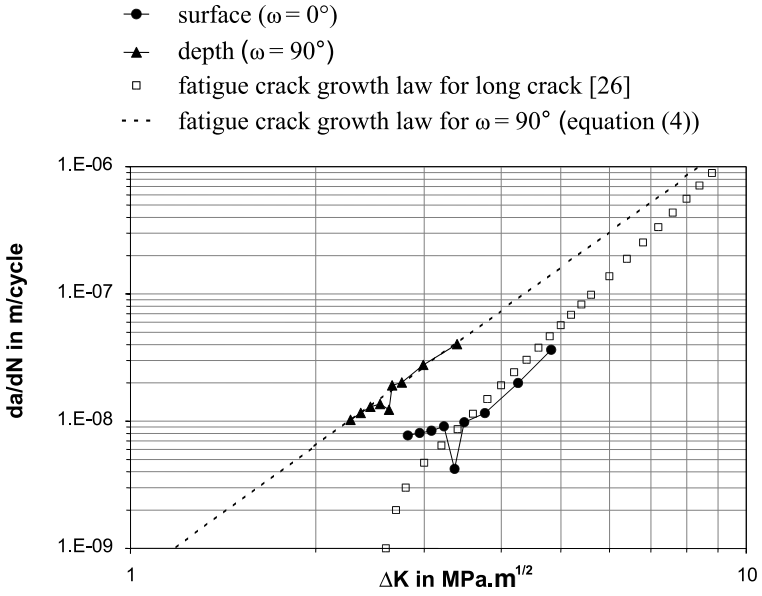

Fig. 6. The fatigue crack growth rates measured at the surface ($\omega = 0°$) and at the deepest point ($\omega = 90°$) of the crack are represented by plain black points and plain triangles, respectively. The sudden drops between 18,000 and 20,000 cycles correspond to post-overload retardation. The fatigue crack growth law measured for a CT specimen in Ref. [19] is given for comparison.

fatigue crack growth law obtained on CT specimens by Venkateswara Rao and Ritchie [26] for the same material is also represented by open squared symbols in Fig. 6.

A discrepancy between the fatigue crack growth rate measured at the surface and in the bulk can be observed in Fig. 6: the slopes of the two curves $da/dN = f(\Delta K)$ and $dc/dN = f(\Delta K)$ are similar but the former is shifted towards lower values of ΔK. Thus for the same ΔK, the crack propagates faster in the bulk than at the surface implying that, at least for the specimen geometry used here, the crack growth behaviour is anisotropic. Thus, a fatigue crack growth law determined at the surface does not account for the crack behaviour in the bulk. Furthermore, if used for fatigue life calculation, the surface experimental law would lead to a non-conservative prediction.

3.3. Overload

After the acquisition of the tomographic scan at 18,000 cycles, a 100% tensile overload was applied to the sample. In Figs. 5(d) and (e), it can be seen that, during the 2000 cycles following the overload, the crack growth is considerably reduced, especially at the surface where the crack propagates three time less than in the bulk.

This discrepancy between retardation at the surface and in the bulk can be quantified by measuring the amplitude of crack retardation on the fatigue crack growth rate curves displayed in Fig. 6. Both curves exhibit a sudden drop between 18,000 and 20,000 cycles: the $dc/dN = f(\Delta K)$ curve decreases from 9×10^{-9} m/cycle down to 4×10^{-9} m/cycle whereas the $da/dN = f(\Delta K)$ curve only decreases from 1.4×10^{-8} m/cycle to 1.26×10^{-8} m/cycle. After cycle 20,000, the crack growth rate recovers its original trend. From this it can be concluded that post-overload retardation appears to be more important at the surface than in the bulk.

4. Simulation of the 3D crack propagation

In the previous section it has been shown that crack propagation at the point ($\omega = 90°$) furthest into the bulk is faster than at the surface ($\omega = 0°$). The objective of this section is to investigate the possibility of modelling crack growth anisotropy in order to predict more precisely the evolution of the crack front shape in the bulk.

4.1. Analytical and numerical simulation of crack propagation with a single crack growth law

The discrepancy between the fatigue crack growth rates at the surface and in the bulk allows us to conclude that a unique crack growth law (e.g., with unique coefficients C and m for the Paris law) cannot be used to predict the evolution of the crack front shape in 3D. It will indeed be necessary to establish a "3D crack propagation law" to simulate anisotropic crack propagation.

However, as a preliminary study, we will simulate crack propagation by integrating the same Paris law over the crack front, as is usually done in crack simulation. By doing so, it will be possible to determine if the discrepancy between simulated and real crack shape is localised at the sample surface or if it affects the whole crack front. The law used for simulation is the fatigue crack growth law measured for $\omega = 90°$. This law, defined by Eq. (4) and represented by a dotted line in Fig. 6, has been chosen for the basis of the modelling, rather than the "surface" law, because numerical calculations of the stress intensity factors are more reliable in the bulk than at the surface. (This point is discussed in Section 5.)

$$\frac{da(\omega)}{dN} = C \cdot [K_{max}(\omega) - K_{min}(\omega)]^m \quad \text{with } C = 10^{-9.2} \text{ and } m = 3.5. \tag{4}$$

In Eq. (4), $K_{max}(\omega)$ and $K_{min}(\omega)$ are the values of the local stress intensity factor calculated at a given point of the crack front localised by the angle ω. The constants C and m have been determined from the $da/dN = f(\Delta K)$ curve in Fig. 6 but without considering the points between cycles 18,000 and 20,000 which are characteristic of post-overload retardation. In the following section, the evolution of the crack front shape between cycles 14,000 and 18,000 will be simulated using both X-FEM (cf. Section 2.6) and an analytical method based on the assumption that the crack front shape is exactly semi-elliptical.

In the numerical simulation, the stress intensity factors are calculated along the crack front using the X-FEM, taking into account the measured 3D crack geometry. The evolution of $K_{max}(\omega)$ along the crack front is obtained by fitting the "raw" numerical values with a polynomial function. Note that the values of $K_{max}(\omega)$ calculated at the first points located just under the sample surface are not taken into account in the polynomial interpolation. The local crack extension $da(\omega)$ is normal to the crack front and its value is calculated at each node by integrating the crack growth law defined by Eq. (4). The new crack front location is calculated for a difference in number of cycles $dN = 4000$. The initial crack is the experimental crack at cycle 14,000 obtained from the first tomographic scan.

In the analytical simulation, the simulated crack front is assumed to be a perfect semi-ellipse: the crack extension $da(\omega)$ is calculated by integrating Eq. (4) only at the two points located at $\omega = 0°$ and $\omega = 90°$. The values of $K_{max}(0°)$ and $K_{max}(90°)$ are obtained from the Newman and Raju equations for a semi-elliptical crack in tension [36]. The initial crack is a semi-ellipse where a and c are the crack size at $\omega = 0°$ and $\omega = 90°$, respectively, as measured on the experimental crack at cycle 14,000.

4.2. Comparison between the simulated and experimental crack front shapes

In the following analysis the simulated crack front obtained using analytical values of K is called the "analytical crack front" and the crack front simulated with the numerical method is called the "numerical crack front".

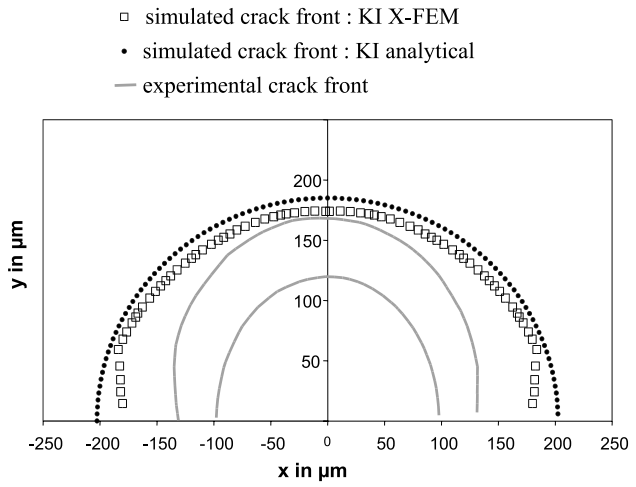

Fig. 7. Simulation of crack propagation using a single Paris law given by Eq. (4) between cycles 14,000 and 18,000. The crack represented by open squared symbols corresponds to the numerical simulation using the stress intensity factors given by the X-FEM. The crack represented by black points is obtained by "analytical simulation" using the Raju and Newman equations to calculate the stress intensity factors.

The experimental crack fronts extracted from the tomographic images (solid lines), the numerical crack front (open squared symbols) and the analytical crack front (filled circles) are compared in Fig. 7. This figure shows that the shape of the numerical crack front, obtained without any shape assumption, is comparable to the perfect semi-ellipse obtained with the analytical method (except for $0° < \omega < 15°$). The discrepancy between the "experimental" and "simulated" crack fronts, both analytical and numerical, is a maximum at the surface and tends to decrease towards the bulk. The crack size for $\omega = 90°$ is overestimated only by 3% in the numerical simulation and by 10% in the analytical simulation. The crack size at the surface is overestimated by 35% in the analytical simulation and by 25% in the numerical simulation. From this it can be concluded that the discrepancy between the simulated and experimental crack shapes, when integrating a unique law over the whole crack front, is not local but affects the shape of the entire crack between $\omega = 0°$ and $\omega = 180°$. This discrepancy is more important when the crack is described as a perfect semi-ellipse than when the real crack shape is taken into account.

4.3. Numerical simulation using a 3D effective crack growth law

One possible reason for the observed crack growth anisotropy between the surface and the bulk is the variation of the closure stress along the crack front: the crack will then propagate faster in the bulk because the closure stress in this region of the crack front is smaller and hence the effective driving force is higher than at the surface. The validity of this assumption as well as the 3D nature of the closure phenomena are discussed in Section 5.

The objective of this section is to establish a 3D crack propagation law that accounts for the crack growth anisotropy induced by closure. The local crack extension $da(\omega)$ will be correlated with an effective stress intensity factor $\Delta K_{\text{eff}}(\omega)$ that takes into account the 3D variation of the closure stress along the crack front.

Elber [37] proposed a modified Paris equation to account for the effect of closure on the crack growth rate: $da/dN = C(\Delta K_{\text{eff}})^m$ where $\Delta K_{\text{eff}} = (K_{\max} - K_{\text{op}})$ is the effective stress intensity factor range and K_{op} is the stress intensity factor at which the crack opens. To account for the variation of the closure stress along the crack, we will modify Elber's equation by introducing a new variable ω such that da/dN and ΔK_{eff} vary along the crack front: $da(\omega)/dN = C(\Delta K_{\text{eff}}(\omega))^m$.

As a first approach, the variation of $K_{\text{op}}(\omega)$ is taken to be linear with the angle ω and is therefore given by $K_{\text{op}}(\omega) = a \cdot \omega + b$. The value of the constants a and b are determined from the values of K_{op} at the surface $K_{\text{op}}(0°)$ and at the deepest point $K_{\text{op}}(90°)$. Data from the literature are used to determine $K_{\text{op}}(0°)$: the closure response of an Al–Li powder metallurgy alloy, very similar to the alloy studied here, was investigated in Ref. [26]. The value of K_{op} measured at the surface of CT specimens, for $R = 0.1$, is found to be equal to $0.4K_{\max}$. We assume here that the ratio $K_{\text{op}}(\omega = 0°)/K_{\max}$ remains constant during the fatigue test and that there is no closure at the deepest point for $\omega = 90°$, which gives $K_{\text{op}}(90°) = 0.1K_{\max}(90°)$. The evolution of the closure stress along the crack front is given by the linear relation

$$K_{\text{op}} = -\frac{0.6K_{\max}}{\pi} \cdot \omega + 0.4K_{\max} \tag{5}$$

The 3D crack growth law taking into account the variation of the closure stress along the crack front is given by

$$\frac{da(\omega)}{dN} = C\left[\left(\frac{0.6}{\pi}\omega + 0.6\right)K_{\max}\right]^m \tag{6}$$

In Eqs. (5) and (6), the angle ω, expressed in radians, is defined for $[0, \pi/2]$ and $K_{\max}(\omega)$ is obtained from a polynomial interpolation of the values calculated by the X-FEM as described in the previous section.

The crack propagation is simulated, using Eq. (6), between 14,000 and 24,000 cycles by calculating the location of the simulated crack front every 2000 cycles. The initial crack front is the crack front at 14,000 cycles obtained from the tomographic images (see Fig. 8(a)). The local crack extension values $da(\omega)$ are calculated along this initial crack front for $dN = 2000$ to predict the location of the crack front at 16,000 cycles (open triangles in Fig. 8(a)). The process is iterated as follows. The $da(\omega)$ values are calculated along the simulated crack front at step N (black triangles) to establish the location of the crack front at step $(N + dN)$ (open triangles). The obtained simulated crack fronts are compared to the experimental crack front (plain grey lines) in Figs. 8(b) and (d). However, as Eq. (6)

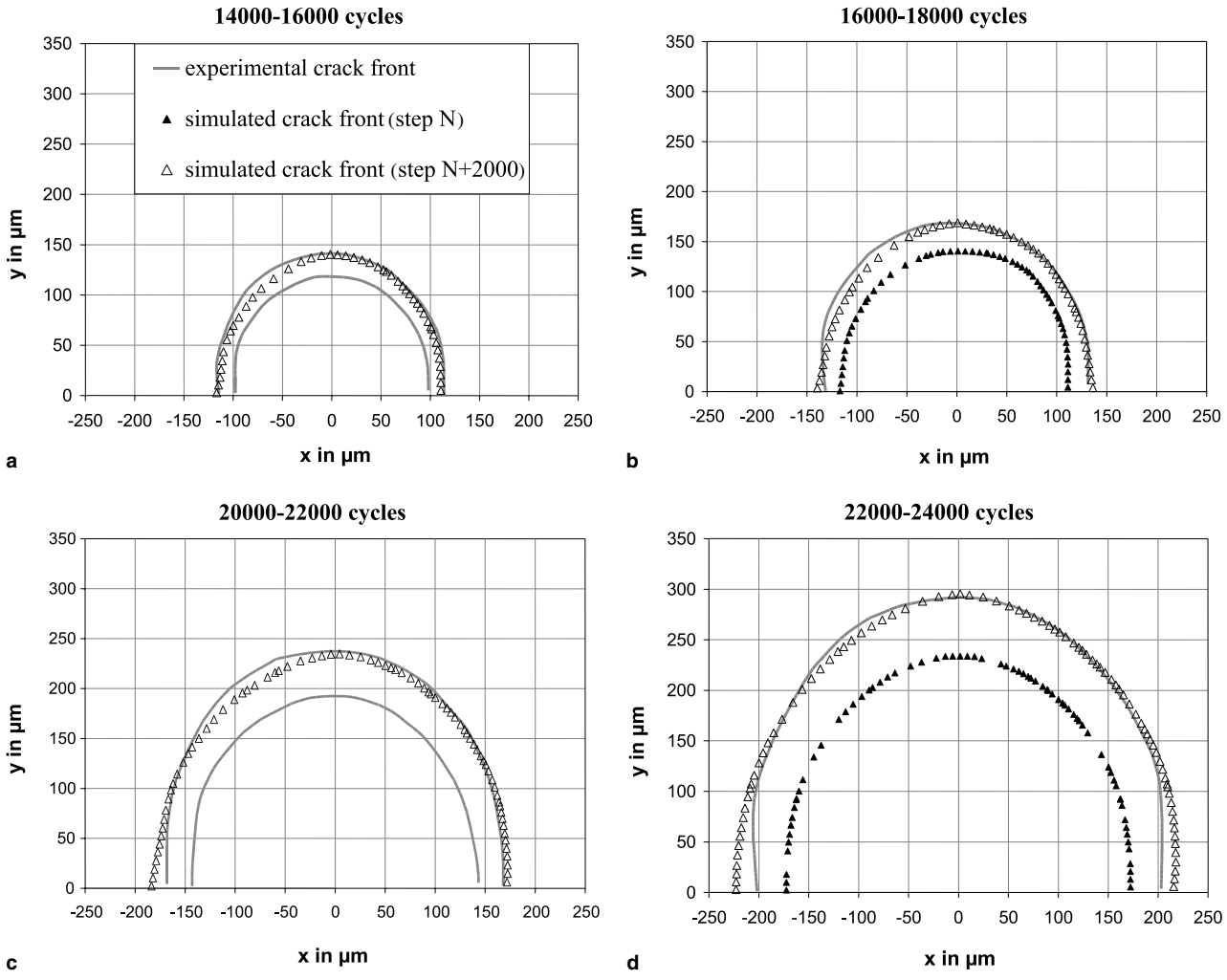

Fig. 8. (a)–(d) The plain grey lines represent the location of the experimental crack front obtained from the tomographic image. The open triangles represent the simulated crack fronts obtained by integrating, for 2000 cycles, the 3D crack growth law defined by Eq. (6). (a, c) The initial crack front used for propagation is the experimental crack front after 14,000 and 20,000 cycles, respectively. (b, d) The initial crack front used for propagation is the simulated crack front (black triangles) that correspond to 16,000 and 22,000 cycles, respectively.

does not model the crack retardation induced by the overload, crack propagation is not simulated between 18,000 and 20,000 cycles. The experimental crack front at step 20,000 cycles is, hence, used to predict the shape of the crack front at step 22,000 and 24,000 cycles (see Figs. 8(c) and (d)).

In Figs. 8(a)–(d), the simulated and experimental crack front shapes appear to be very similar even in the region close to the sample surface: in this region the average error between simulated and experimental crack size is 6%, whereas at the depth the error is less than 2%. These values are far less than the error found between experimental and simulated crack sizes calculated using a single Paris law as described in the previous section. It can thus be concluded that the 3D crack propagation law, based on a linear variation of K_{op} along the crack front, gives a good prediction of the crack growth, at least for the crack/sample geometry considered in this study.

5. Discussion

5.1. Long crack behaviour and applicability of LEFM

The approach presented in this study relies on the assumption that small-scale yielding conditions apply despite the physically short dimensions of the crack (100–500 µm). This assumption seems justified since the estimated monotonic plastic zone size is "small" compared to the crack size. Indeed, the ratio of the monotonic plastic zone size r_p and the crack size has been calculated at the surface r_{pc}/c (assuming plane stress conditions) and in the bulk r_{pa}/a (assuming plane strain conditions). For the crack length considered in this study the values range between $0.09 < r_{pc}/c < 0.13$ and $0.016 < r_{pa}/a < 0.018$. At the surface, these values are rather high but remain acceptable. In the bulk, they seem to conform well to the applicability limits of LEFM that can be found in

the literature [38]. It seems therefore reasonable to correlate the stress intensity factor range calculated along the crack front with the fatigue crack growth rate. It should be remembered that the values of the stress intensity factors at the free surface/crack intersection calculated with numerical methods should be treated cautiously and are usually obtained, as already mentioned by several authors, by extrapolating values calculated "inside" the sample [39,40].

5.2. Crack growth rate anisotropy between surface and bulk

Concerning the observed anisotropy between the fatigue crack growth rates measured at the surface and in the bulk, two remarks can be made. First, the fatigue crack growth rate measured at the surface of the studied sample is close to the fatigue crack growth rate obtained for long cracks in conventional CT specimens [26]. This result suggests that the crack propagation observed on a small sample is representative of the long crack behaviour described by LEFM in larger samples of standard geometry.

Second, the crack propagates faster in the bulk than at the surface. Such crack growth anisotropy has already been observed in 7075-T651 Al alloy for semi-elliptical cracks by McDonald and Daniewicz [41]. To account for these results, Solanki et al. have established a "local" Paris law, defined by local coefficients C_i and m_i [42]. The values of C_i and m_i were deduced by linear interpolation between the experimental values of C and m, measured in the depth and at the free surface. However, in our case, crack propagation is expected to be isotropic as the grain structure of the Al–Li alloy studied is ultrafine and equiaxed and possesses no crystallographic texture. Thus, there is no "physical" justification for allowing the C and m coefficients to vary along the crack front as they are intrinsic material parameters. As mentioned in Section 4.1, it was therefore assumed in this study that crack closure is the origin of the observed crack growth anisotropy.

5.3. 3D nature of closure: experimental results

As conventional methods of closure stress measurements are all surface measurements, the experimental characterisation of the 3D nature of closure phenomena is a difficult task which requires the development of specific methods to evaluate the contribution of surface and bulk to the global closure response of the material. Qualitative results have been obtained for instance in Refs. [43,44]: specimens were sectioned normally to the crack propagation plane to observe directly the crack front through the specimen thickness. These experiments confirm the fact that the closure stress is higher at the surface than in the bulk. This phenomenon has been attributed to the variation of constraint along the crack front: plane stress conditions prevail at the surface which implies a larger plastic zone size, and thus more closure than in the bulk, where plane strain conditions prevail (a trend reflected by the values of r_{pa}/a and r_{pc}/c given previously). The difference between the closure stress at the surface and in the bulk has been determined quantitatively using a fractographic method developed by Pelloux et al. [45]. This technique relies on the assumption that fatigue striation spacing is directly affected by the closure stress which can hence be determined by comparing different striation spacings induced by a special load sequence of varying amplitude. This technique has been used to investigate the 3D closure behaviour of through cracks, as for instance in Refs. [46,47] and part-through cracks in Ref. [9]. In this latter paper, Putra et al. measure the evolution of the opening stress, $S_{op} = f(\phi)$, along the crack front of semi-elliptical cracks in 7075 T6 Al alloy (the angle ϕ used in Ref. [9] has the same meaning as ω used in the present paper). However, as fatigue striations close to the sample surface are not well defined, this fractographic method does not allow the determination of values of S_{op} between $\phi = 0°$ and $\phi = 15°$ (which corresponds to a thickness of 25–50 μm for the crack size range observed in our experiment). In the bulk, experimental values of S_{op} decrease linearly between $\phi = 15°$ and $\phi = 90°$, which confirm our assumption, but with a slope that is lower than the one of Eq. (5) used for the simulation.

5.4. 3D FE simulations of plasticity-induced crack closure phenomena

For the particular ultrafine-grained Al alloy used in this study, the main mechanism responsible for closure is plasticity-induced crack closure (PICC) [23]. PICC phenomena for semi-elliptical cracks have been analysed in 3D by the FE method [48–52]. 3D elastic–plastic FE simulations show that the loading part of the fatigue cycle can be described as a "continuous unzipping process" during which the crack opens first in the bulk. They also confirm the fact that S_{op} is higher at the surface than in the bulk. In Ref. [49], the evolution of the closure stress has been calculated: the obtained $S_{op} = f(\omega)$ curve does not follow the linear trend of Eq. (5) used in this study but decreases between $\omega = 0°$ and $\omega = 10°$ and then remains at a constant value for $10° < \omega < 90°$. As the crack/sample size ratio of the sample used in Ref. [49] is 10 times less than for our sample, this difference might be due to the influence of the state of stress as will be explained in the next section. It should also be emphasised that numerical values of S_{op} are greatly influenced by the mesh refinement as well as the crack node release scheme used in the FE simulation as mentioned in Ref. [50].

5.5. Influence of the state of stress on the 3D closure behaviour

The influence of the state of stress on the variation of S_{op} has been studied for through cracks by comparing elastic–plastic FE calculations performed on thin and thick MT samples [53] (the thickness ratio between the thick and the thin sample being 7.5). It was found that,

in thin MT samples, where plane stress conditions prevail, S_{op} decreases linearly between the sample surface and the centre of the specimen. For thicker MT samples, the evolution is different: S_{op} decreases quickly in a region located just under the sample surface and then remains at a constant value in the central part of the sample where plane strain conditions prevail. It can be concluded that for through cracks, the variation of S_{op} along the crack front is linear only when plane stress conditions prevail in the whole sample. In our case, as the studied crack is not a through crack but a part-through crack, direct comparison is difficult. However, the results obtained in Ref. [53] seem to explain the difference, mentioned in the previous paragraph, between the $S_{op} = f(\omega)$ curve obtained by FE calculation for a large sample [49] and the linear equation (5) used in the simulation. It can thus be concluded that the influence of the state of stress on the variation of S_{op} along the crack front should be taken into account, which implies that Eq. (5) should be modified whenever a different crack/sample geometry is considered.

5.6. Overload

It has been shown in Section 3.3 that crack retardation following the 100% overload varies along the crack front: it is maximum at the surface for ($\omega = 0°$) and decreases towards the bulk to a minimum value for ($\omega = 90°$). The fact that post-overload retardation occurs mainly at the surface has been observed on fracture surfaces, but only for through cracks in Refs. [54,55].

Retardation induced by a tensile overload can be attributed to different mechanisms such as compressive residual stress, branching and also PICC [56]. In the fine-grained alloy studied here, PICC is the main mechanism responsible for post-overload crack retardation [23]. The fact that crack retardation occurs mainly at the surface, as described above, implies that PICC is more important and, hence, the value of K_{op} higher at the surface than in the bulk. This result is consistent with the assumption made in Section 4.2 that $K_{op}(0°) > K_{op}(90°)$ which was used to establish the 3D crack growth law.

6. Conclusions

The 3D propagation of a semi-elliptical fatigue crack in an ultrafine-grained Al–Li alloy has been visualised in situ using synchrotron radiation X-ray microtomography. This technique can be used to perform in situ characterisation of fatigue cracks in the bulk of opaque materials at a resolution close to 1 μm, which is relevant for studying crack propagation. It should be emphasised that the 3D images of the cracks have been obtained without changing the load cycles or the environmental conditions contrary to what is achieved with classic post-mortem fractography techniques. However, the stringent resolution requirements for detection of crack opening displacements at the submicrometre level limit the field of view to about 1 mm and hence imply the adoption of special sample geometries with dimensions in the millimetric range.

The experimentally observed 3D crack propagation has been modelled using LEFM concepts: the local crack growth rate measured in the bulk is correlated with the stress intensity factor range ΔK calculated using the X-FEM taking into account the real 3D geometry of the crack obtained from the tomographic images. It has been shown that:

- Crack growth rates measured at the surface of the small sample used in our experiment are similar to those obtained on large conventional fatigue samples for the same alloy.
- The experimentally observed semi-elliptical crack propagates faster in the bulk than at the surface.
- Variation of the closure stress along the crack front can account for the observed crack growth anisotropy between surface and bulk. As PICC is the main mechanism responsible for closure in the alloy studied here, a larger plastic zone size at the surface (plane stress) can explain a higher closure stress than in the bulk, where plane strain conditions limit the development of plasticity and hence closure.
- Assuming that the variation of the closure stress between surface and bulk is linear, a 3D crack growth law equation has been established to simulate crack propagation. The predicted and experimental crack shapes, compared at different stages, appear to be very similar.

This means that, for the sample geometry investigated here, a single Paris law can be used to predict the observed crack growth anisotropy provided the variation of the closure stress along the crack front is taken into account.

From a more general point of view, this study has shown that coupling X-ray microtomography to X-FEM provides a promising tool to assess the 3D behaviour of arbitrary shaped cracks and to perform direct comparisons of "experimental" and "simulated" crack shapes during propagation. Such data, to the best of the authors' knowledge, are currently lacking in the literature.

Acknowledgements

The authors are grateful to Mr. Bultreys from FEI Europe for machining the notch with the help of a FEI dual-beam FIB/SEM system and to Ian Sinclair for fruitful discussions on the 3D nature of the closure phenomenon. We also like to thank Andy Tarrant of Aerospace Metal Composites Ltd for providing the material. The ESRF and staff are acknowledged for their help and assistance during the tomographic imaging experiment.

References

[1] Enmark M, Lucas G, Odette GR. J Nucl Mater (The Netherlands) 1992:1038–41.
[2] Makoto A, Masumi S. Eng Fract Mech 2005;72:319–34.

[3] Knight MJ, Brennan FP, Dover WD. NDT&E Int 2004;37:337–43.
[4] Zerwer A, Polak MA, Santamarina JC. J Struct Eng 2001;128:240–8.
[5] Ravichandran AS, Larsen JM. Mater Sci Eng A 1992;153:499–507.
[6] Forman RG, Mettu SR. ASTPM STP 1131 1992;1:519–46.
[7] Nadot Y, Ranganathan N, Mendez J, Béranger AS. Scr Mater 1997;37:549–53.
[8] Husset J, Lieurade HP, Maltrud F, Truchon M. Welding in the World/Soudage dans le Monde 1985;23:276–83.
[9] Putra IS, Schijve J. Fatigue Fract Eng Mater Struct 1992;15:323–38.
[10] McFadyen NB, Bell R, Vosikovsky O. Int J Fatigue 1988;10:47–9.
[11] Forman RG, Shivakumar V. ASTM STP 905 1986:59–74.
[12] Scott PM, Thorpe TW. Fatigue Eng Mater Struct 1981;4:291–309.
[13] Pommier S, Sakae C, Murakami Y. Int J Fatigue 1999;21:243–51.
[14] Fatigue crack growth computer program "Nasgro" version 3.0. Reference manual. March; 2002.
[15] Wawrzynek PA, Martha LF, Ingraffea AR. In: Rosakis AJ et al., editors. Analytical, numerical and experimental aspects of three dimensional fracture processes, AMD-vol. 91. New York (NY): ASME; 1988. p. 321–7.
[16] Fulland M, Richard HA. Steel Res 2003;74:584–90.
[17] Wessel C, Cisilino A, Santi O, et al. Theor Appl Fracture Mech 2001;35:47–58.
[18] Riddell WT, Ingraffea AR, Wawrzynek PA. Eng Fract Mech 1997;58:293–310.
[19] Ludwig W, Buffière JY, Savelli S, Cloetens P. Acta Mater 2003;51:585–98.
[20] Marrow TJ, Buffière JY, Withers PJ, Johnson G, Engelberg D. Int J Fatigue 2003;26:717–25.
[21] Miller KJ. Fatigue Eng Mater Struct 1982;5:223–32.
[22] Pitcher PD, Bushby RS, Vine WJ, Smith AF, Tarrant AD. Mater Sci Technol 2001;17:807–14.
[23] Bray GH, Reynolds AP, Starke EA. Metall Trans A 1992;23:3055–66.
[24] Bray GH, Kaisand LR, Starke EA. Fatigue Fracture Eng Mater Struct 1995;18:551–64.
[25] Vine WJ, Pitcher PD, Tarrant AD. Mater Sci Technol 2001;17:645–50.
[26] Venkateswara Rao KT, Ritchie RO. Metall Trans A 1991;22:191–202.
[27] Sinclair I. Private communication. Unpublished work, School of Engineering University of Southampton, UK; 2005.
[28] Cloetens P, Pateyron-Salomé M, Buffière JY, Peix G, Baruchel J, Peyrin F. J Appl Phys 1997;81:58–78.
[29] Buffière JY, Ferrié E, Proudhon H, Ludwig W. Mater Sci Technol [in press].
[30] Amira 3.1. Mercury Computer System GmbH, Lepiusstr., 70 D-12163 Berlin, Germany. Available from: http://www.amiravis.com/.
[31] Belytschko T, Black T. Int J Numer Meth Eng 1999;45:601–20.
[32] Osher S, Sethian JA. J Comput Phys 1988;79:12–49.
[33] Moes N, Dolbow J, Belystchko T. Int J Numer Meth Eng 1999;46:131–50.
[34] Gravouil A, Moes N, Belytschko T. Int J Numer Meth Eng 2002;53:2569–86.
[35] Gosz M, Moran B. Eng Fract Mech 2002;69:299–319.
[36] Newman JC, Raju IS. ASTM STP 791 1983:238.
[37] Elber W. Eng Fract Mech 1970;2:37–45.
[38] Anderson TL. Fracture mechanics – fundamentand and applications. 2nd ed. Boca Raton, (FL): CRC Press; 1995.
[39] Smith RA, Cooper JF. Int J Press Ves 1989;36:326–35.
[40] Lin XB, Smith RA. Eng Fract Mech 1999;69:503–22.
[41] McDonald Jr V, Daniewicz SR. ASTM STP 1406 2001:381–96.
[42] Solanki K, Daniewicz DR, Newman Jr JC. Eng Fract Mech 2004;71:149–71.
[43] Lyndley TC, Richards CE. Mater Sci Eng 1974;14:281–93.
[44] Fleck NA, Smith RA. Int J Fatigue 1982;4:157–60.
[45] Pelloux RM, Faral M, Mc Gee WM. Fatigue Eng Mater Struct 1979:21–35.
[46] Dawicke DS, Grandt AF, Newman JC. Eng Fract Mech 1990;36:11–121.
[47] Sunder S, Dash K. Int J Fatigue 1992;3:97–105.
[48] Chermahini RG, Palmberg B, Blom AF. Int J Fatigue 1993;4:259–63.
[49] Skinner JD, Daniewicz SR. Eng Fract Mech 2002;69:1–11.
[50] Solanki K, Daniewicz SR, Newman JC. Eng Fract Mech 2004;71:149–71.
[51] Hou CY. Int J Fatigue 2004;26:1225–39.
[52] Zhang JZ, Bowen P. Eng Fract Mech 1998;60:341–60.
[53] Chermahini RG, Shivakumar KN, Newman Jr JC, Blom AF. Eng Fract Mech 1989;34:393–401.
[54] Matsuoka S, Tanaka K. Eng Fract Mech 1980;13:293–306.
[55] Bathias C, Baïlon JP. In: Hermès, editor. La fatigue des matériaux et des structures; 1997.
[56] Suresh S. Eng Fract Mech 1983;18:577–93.